The Astrophysical Journal, 937:10 (11pp), 2022 September 20 https://doi.org/10.3847/1538-4357/ac8c28
© 2022. The Author(s). Published by the American Astronomical Society.
OPEN ACCESS

Stratified Distribution of Organic Molecules at the Planet-formation Scale in the HH 212 Disk Atmosphere

Chin-Fei Lee[1,2], Claudio Codella[3,4], Cecilia Ceccarelli[4], and Ana López-Sepulcre[4,5]
[1] Academia Sinica Institute of Astronomy and Astrophysics, P.O. Box 23-141, Taipei 106, Taiwan; cflee@asiaa.sinica.edu.tw
[2] Graduate Institute of Astronomy and Astrophysics, National Taiwan University, No. 1, Sec. 4, Roosevelt Road, Taipei 10617, Taiwan
[3] INAF, Osservatorio Astrofisico di Arcetri, Largo E. Fermi 5, I-50125 Firenze, Italy
[4] Univ. Grenoble Alpes, CNRS, Institut de Planétologie et d'Astrophysique de Grenoble (IPAG), F-38000 Grenoble, France
[5] Institut de Radioastronomie Millimétrique (IRAM), 300 rue de la Piscine, F-38400 Saint-Martin d'Hères, France
Received 2022 May 8; revised 2022 August 22; accepted 2022 August 22; published 2022 September 16

Abstract

Formamide (NH_2CHO) is considered an important prebiotic molecule because of its potential to form peptide bonds. It was recently detected in the atmosphere of the HH 212 protostellar disk on the solar system scale where planets will form. Here we have mapped it and its potential parent molecules HNCO and H_2CO, along with other molecules CH_3OH and CH_3CHO, in the disk atmosphere, studying its formation mechanism. Interestingly, we find a stratified distribution of these molecules, with the outer emission radius increasing from ∼24 au for NH_2CHO and HNCO, to 36 au for CH_3CHO, to 40 au for CH_3OH, and then to 48 au for H_2CO. More importantly, we find that the increasing order of the outer emission radius of NH_2CHO, CH_3OH, and H_2CO is consistent with the decreasing order of their binding energies, supporting that they are thermally desorbed from the ice mantle on dust grains. We also find that HNCO, which has much lower binding energy than NH_2CHO, has almost the same spatial distribution, kinematics, and temperature as NH_2CHO, and is thus more likely a daughter species of desorbed NH_2CHO. On the other hand, we find that H_2CO has a more extended spatial distribution with different kinematics from NH_2CHO, thus questioning whether it can be the gas-phase parent molecule of NH_2CHO.

Unified Astronomy Thesaurus concepts: Star formation (1569); Star forming regions (1565); Stellar accretion disks (1579); Astrochemistry (75); Interstellar molecules (849)

1. Introduction

Formamide (NH_2CHO) is an interstellar complex organic molecule (iCOM, referring to C-bearing species with six atoms or more; Herbst & van Dishoeck 2009; Ceccarelli et al. 2017) and a key precursor of more complex organic molecules, that can lead to the origin of life, because of its potential to form peptide bonds (Saladino et al. 2012; Kahane et al. 2013; López-Sepulcre et al. 2019). It has been detected in the gas phase in hot corinos (Kahane et al. 2013; Coutens et al. 2016; Imai et al. 2016; López-Sepulcre et al. 2017; Bianchi et al. 2019; Hsu et al. 2022), which are the hot ($\gtrsim$100 K) and compact ($\lesssim$100 au) regions immediately around low-mass (Sun-like) protostars (Ceccarelli et al. 2007). The formamide origin is still under debate. In principle, formamide could be synthesized on the grain surfaces or in the gas phase. Two routes have been proposed in the first case: the hydrogenation of HNCO (Charnley & Rodgers 2008) and the combination of the HCO and NH_2 radicals, when they become mobile upon the warming of the dust by the protostar. However, the first route has been challenged by both experiments (Noble et al. 2015) and quantum chemical (QM) calculations (Song & Kastner 2016). Later, the hydrogenation of HNCO is found to be feasible and followed by H abstraction of NH_2CHO in a dual-cycle consisting of H addition and H abstraction (Haupa et al. 2019). The second route (i.e., the combination of HCO and NH_2) has also been challenged by QM calculations (Rimola et al. 2018) and found possible, even though it can also form NH_3+CO in competition with the formamide (Enrique-Romero et al. 2022). In the gas-phase formation theory, it has been proposed that formamide is formed by the gas-phase reaction of H_2CO with NH_2 (Kahane et al. 2013). This hypothesis was later challenged by Song & Kastner (2016). Nonetheless, QM computations (Vazart et al. 2016; Skouteris et al. 2017) coupled with astronomical observations in shocked regions (Codella et al. 2017) support this hypothesis. In the same vein, the observed deuterated isomers of formamide (including NH_2CDO, cis- and trans-NHDCHO; Coutens et al. 2016) fit well with the theoretical predictions of a gas-phase formation route (Skouteris et al. 2017). On the other hand, the observed high deuterium fractionation of ∼2% for the three different forms of formamide (NH_2CDO, cis- and trans-NHDCHO) could also be consistent with the formation in ice mantles on dust grains.

The hot corino in the HH 212 protostellar system (Codella et al. 2016) in Orion at a distance of ∼400 pc is particularly interesting because recent observations have spatially resolved it and found it to be an atmosphere of a solar system scale protostellar disk around a protostar (Lee et al. 2017c). This disk atmosphere is rich in iCOMs (Lee et al. 2017c; Codella et al. 2018; Lee et al. 2019), including formamide. More importantly, these iCOMs have a relative abundance similar to that of other hot corinos (Cazaux et al. 2003; Imai et al. 2016; López-Sepulcre et al. 2017; Bianchi et al. 2019; Manigand et al. 2020), and even comets (Biver et al. 2015). Therefore, the study of formamide in protostellar disks is key to investigating the emergence of prebiotic chemistry in nascent planetary bodies. In this paper we will study the origin and formation pathways of formamide in this protostellar disk.

Original content from this work may be used under the terms of the Creative Commons Attribution 4.0 licence. Any further distribution of this work must maintain attribution to the author(s) and the title of the work, journal citation and DOI.

Previously, the HH 212 disk was mapped at a wavelength $\lambda \sim 0.85$ mm (Lee et al. 2017c) covering one NH_2CHO line. Here we map it at a longer wavelength $\lambda \sim 1.33$ mm, with spectral windows set up to cover more NH_2CHO lines in order to derive the physical properties of NH_2CHO. This setup also covers the lines of HNCO and H_2CO, which have not been reported before, in order to investigate the formation pathways of NH_2CHO. At a longer wavelength, since the continuum emission of the disk is optically thinner, we can also map the molecular line emission in the disk atmosphere closer to the midplane and the central source. Moreover, the deuterated species and ^{13}C isotopologue of H_2CO are also detected, allowing us to constrain the origin and correct the optical depth of H_2CO, respectively. In addition, CH_3OH and CH_3CHO are also detected, allowing us to further constrain the formation mechanism of NH_2CHO. More importantly, with the recently updated binding energies of these molecules, we can investigate the formation mechanism of these molecules and the chemical relationship among them.

2. Observations

The HH 212 protostellar disk was observed with Atacama Large Millimeter/submillimeter Array (ALMA) in Band 6 centered at a frequency of ~226 GHz (or $\lambda \sim 1.33$ mm) in Cycle 5. Project ID was 2017.1.00712.S. Two observations were executed. One was executed on 2017 October 04 in C43-9 configuration with 46 antennas for ~18 minutes on source with a baseline length of 41.4 m to 15 km to achieve an angular resolution of ~0.″02. The other was executed on 2017 December 31 in C43-6 configuration with 46 antennas for 9 minutes on source with a baseline length of 15.1 m to 2.5 km to recover a size scale up to ~1.″8, which is four times the disk size. The correlator was set up to have four spectral windows (centered at 232.005, 234.005, 217.765, and 219.705 GHz), each with a bandwidth of 1.875 GHz and 1920 channels, and thus a spectral resolution of 0.976 MHz per channel, corresponding to ~1.3 km s^{-1} per channel. The primary beam was ~25″, much larger than the disk size.

The data were calibrated with the CASA package version 5.1.1, with quasar J0423-0120 (a flux of ~0.93 Jy) as a passband and flux calibrator, and quasar J0541-0211 (a flux of ~0.096 Jy) as a gain calibrator. Line-free channels were combined to generate a visibility for the continuum centered at 226 GHz. We used a robust factor of −1.0 for the visibility weighting to generate the continuum map with a synthesized beam of $0.''021 \times 0.''016$ at a position angle of ~79°. The noise level is ~20 μJy $beam^{-1}$ or 1.4 K. The channel maps of the molecular lines were generated after continuum subtraction. Using a visibility weighting of 0.5, the synthesized beam has a size of $0.''055 \times 0.''042$ at a position angle of ~49°. The noise levels are ~0.9 mJy $beam^{-1}$ (or ~10 K) in the channel maps. The velocities in the channel maps are LSR velocities.

3. Results

The detected lines of NH_2CHO (16 lines), HNCO (7 lines), H_2CO (2 lines) as well as its doubly deuterated species D_2CO (2 lines) and ^{13}C isotopologue $H_2^{13}CO$ (1 line), CH_3OH (12 lines), and CH_3CHO (7 lines) are listed in Table 1. They have upper-level energy $E_u \lesssim 500$ K, but with $E_u < 120$ K for CH_3CHO, H_2CO as well as its deuterated species and isotopologue. In order to increase the sensitivity for better detections, we divided them into two ranges of upper-level energies: $E_u < 120$ K and $E_u > 120$ K, and then stacked them to produce the mean channel maps, and then the total line intensity maps, and the position–velocity (PV) diagrams.

3.1. Stratified Distribution of Molecules

Figure 1 shows the total line intensity maps (red contours) of these molecules on top of the continuum map of the disk at $\lambda \sim 1.33$ mm, in order to pinpoint the location of these molecules in the disk and the chemical relationship among them. As shown in Figure 1(c), the disk is nearly edge-on, with an equatorial dark lane tracing the cooler midplane sandwiched by two brighter features (outlined by the 4th and 5th contour levels) on the top and bottom tracing the warmer surfaces, as seen before in continuum at a shorter wavelength of ~0.85 mm (Lee et al. 2017b).

As can be seen, the emission structure of a given molecule is similar in different E_u ranges, suggesting that it is more dominated by the distribution of the molecule than the upper energy level. After stacking the lines, we achieved a better sensitivity in NH_2CHO than that in the previous observations obtained at higher resolution (Lee et al. 2017c), and detected NH_2CHO not only in the lower disk atmosphere, but also in the upper disk atmosphere. More importantly, we can better pinpoint its emission and find it to be in the inner disk where the disk is warmer. It is brighter in the lower disk atmosphere, with two emission peaks clearly seen on the map with $E_u > 120$ K (see Figure 1(b)). HNCO is detected with the spatial distribution and radial extent consistent with NH_2CHO. Looking back at the previous results of other iCOMs detected at a higher frequency of ~346 GHz (Lee et al. 2019), we find that t-HCOOH was also detected with the spatial distribution and radial extent consistent with NH_2CHO (see Figure 1(f) adopted from Lee et al. 2019). Notice that the radial distribution of molecular gas detected at a higher frequency can also be compared with that here at a lower frequency, because the optical depth of the underlying continuum of the dusty disk mainly affects the vertical distribution (i.e., height) of molecular gas in the atmosphere (see Section 4.1). On the other hand, H_2CO is only detected with $E_u < 70$ K, and its emission extends further out in a radial direction beyond the centrifugal barrier (CB; Figure 1(g)). The emission is also detected at a larger distance from the disk midplane and extends away from the disk atmosphere, overlapping with the base of the SO disk wind (Lee et al. 2021a) and thus tracing the wind from the disk. Its deuterated species D_2CO is detected mainly in the disk atmosphere, also at a larger distance from the midplane and a larger radius from the central protostar than NH_2CHO. On the other hand, the emission of the ^{13}C isotopologue $H_2^{13}CO$ is very faint and mainly detected in the disk atmospheres. CH_3OH is detected in the atmosphere extending out to the CB, as found before (Lee et al. 2017c, 2019). The emission also extends away from the disk midplane, suggesting that part of it also traces the wind from the disk. As for CH_3CHO, the emission is mainly detected in the disk atmosphere and extends radially toward the CB. In summary, NH_2CHO, HNCO, D_2CO, $H_2^{13}CO$, and CH_3CHO trace mainly the disk atmosphere, while H_2CO and CH_3OH trace not only the disk atmosphere, but also the disk wind.

We can also measure the vertical height of these molecules (using lines with $E_u < 120$ K) along the jet axis in the lower atmosphere where the emission is brighter, and find it to be

Table 1
Line Properties from Splatalogue

Transition QNs	Frequency (MHz)	$\log(A_{ul})$ (s^{-1})	E_u (K)	g_u	W[a] (K km s^{-1})	Remarks
NH_2CHO 10(1, 9)- 9(1, 8)	218459.21	−3.126	60.812	21	119	CDMS
NH_2CHO 11(2,10)-10(2, 9)	232273.64	−3.054	78.949	23	120	CDMS
NH_2CHO 11(8, 3)-10(8, 2)	233488.88	−3.360	257.724	23	29^m	CDMS
NH_2CHO 11(8, 4)-10(8, 3)	233488.88	−3.360	257.724	23	29^m	CDMS
NH_2CHO 11(7, 4)-10(7, 3)	233498.06	−3.258	213.124	23	42	CDMS
NH_2CHO 11(7, 5)-10(7, 4)	233498.06	−3.258	213.124	23	42	CDMS
NH_2CHO 11(6, 6)-10(6, 5)	233527.79	−3.186	174.449	23	38	CDMS
NH_2CHO 11(6, 5)-10(6, 4)	233527.79	−3.186	174.449	23	38	CDMS
NH_2CHO 11(5, 7)-10(5, 6)	233594.50	−3.133	141.714	23	56^m	CDMS
NH_2CHO 11(5, 6)-10(5, 5)	233594.50	−3.133	141.714	23	56^m	CDMS
NH_2CHO 11(4, 8)-10(4, 7)	233734.72	−3.093	114.932	23	91	CDMS
NH_2CHO 11(4, 7)-10(4, 6)	233745.61	−3.093	114.933	23	132	CDMS
NH_2CHO 11(3, 9)-10(3, 8)	233896.57	−3.064	94.110	23	91	CDMS
NH_2CHO 11(3, 8)-10(3, 7)	234315.49	−3.062	94.158	23	96	CDMS
HNCO 10(1,10)-9(1, 9)	218981.00	−3.847	101.078	21	212	CDMS
HNCO 10(3, 8)-9(3, 7)	219656.76	−3.920	432.959	21	41^m	CDMS
HNCO 10(3, 7)-9(3, 6)	219656.77	−3.920	432.959	21	41^m	CDMS
HNCO 10(2, 9)-9(2, 8)	219733.85	−3.871	228.284	21	101	CDMS
HNCO 10(2, 8)-9(2, 7)	219737.19	−3.871	228.285	21	121	CDMS
HNCO 10(0,10)-9(0, 9)	219798.27	−3.832	58.019	21	192[b]	CDMS
HNCO 10(1, 9)-9(1, 8)	220584.75	−3.837	101.502	21	198	CDMS
H_2CO 3(0, 3)- 2(0, 2)	218222.19	−3.550	20.956	7	266[b]	CDMS
H_2CO 3(2, 2)- 2(2, 1)	218475.63	−3.803	68.093	7	230	CDMS
D_2CO 4(0,4) - 3(0,3)	231410.23	−3.45914	27.88284	18	67[b]	CDMS
D_2CO 4(2,3) - 3(2,2)	233650.44	−3.57046	49.62595	18	104	CDMS
H_2 ^{13}CO 3(1, 2)- 2(1, 1)	219908.52	−3.59109	32.93810	21	120	CDMS
CH_3OH 5(1) - 4(2) E1 vt = 0	216945.52	−4.915	55.871	11	347[b]	JPL
CH_3OH 6(1) - - 7(2) - vt = 1	217299.20	−4.367	373.924	13	155	JPL
CH_3OH 20(1) -20(0) E1 vt = 0	217886.50	−4.471	508.375	41	89	JPL
CH_3OH 4(2) - 3(1) E1 vt = 0	218440.06	−4.329	45.459	9	263[b]	JPL
CH_3OH 8(0) - 7(1) E1 vt = 0	220078.56	−4.599	96.613	17	347[b]	JPL
CH_3OH 10(-5) -11(-4) E2 vt = 0	220401.31	−4.951	251.643	21	256	JPL
CH_3OH 10(2) - - 9(3) - vt = 0	231281.11	−4.736	165.347	21	240[b]	JPL
CH_3OH 10(2)+- 9(3)+vt = 0	232418.52	−4.729	165.401	21	295[b]	JPL
CH_3OH 18(3)+-17(4)+vt = 0	232783.44	−4.664	446.531	37	214	JPL
CH_3OH 18(3) - -17(4) - vt = 0	233795.66	−4.658	446.580	37	230	JPL
CH_3OH 4(2) - - 5(1) - vt = 0	234683.37	−4.734	60.923	9	285[b]	JPL
CH_3OH 5(-4) - 6(-3) E2 vt = 0	234698.51	−5.197	122.720	11	195[b]	JPL
CH_3CHO 12(4, 8)-11(4, 7) E, vt = 0	231484.37	−3.409	108.289	50	29	JPL
CH_3CHO 12(4, 9)-11(4, 8) E, vt = 0	231506.29	−3.409	108.251	50	111	JPL
CH_3CHO 12(3,10)-11(3, 9) E, vt = 0	231748.71	−3.388	92.510	50	65	JPL
CH_3CHO 12(3, 9)-11(3, 8) E, vt = 0	231847.57	−3.387	92.610	50	46	JPL
CH_3CHO 12(3, 9)-11(3, 8) A, vt = 0	231968.38	−3.383	92.624	50	116	JPL
CH_3CHO 12(2,10)-11(2, 9) E, vt = 0	234795.45	−3.352	81.864	50	54	JPL
CH_3CHO 12(2,10)-11(2, 9) A, vt = 0	234825.87	−3.351	81.842	50	50	JPL

Notes.
[a] Integrated line intensities (see text for the definition) measured from the lower disk atmosphere. Except for CH_3OH, which used the values at the emission peak position, they are the mean values averaging over a rectangular region (with a size of $0\farcs17 \times 0\farcs05$ covering most of the emission) centered at the lower atmosphere. In this column, the line intensities commented with "m" are the mean values obtained by averaging over two or more lines with similar E_u and log A_{ul} for better measurements.
[b] Likely optically thick and thus ignored in the fitting of the rotation diagram and calculation of column density. The line intensities here are assumed to have an uncertainty of 40%.

∼15, 19, 20, 24, and 26 au, respectively for NH_2CHO, HNCO, CH_3CHO, CH_3OH, and H_2CO. We will discuss the vertical height later with the outer radius of these molecules measured from the PV diagrams.

3.2. Kinematics

The spatiokinematic relationship among these molecules can be studied with the PV diagrams cut across the upper and lower disk atmospheres, as shown in Figure 2. Here we use the emission with $E_u < 120$ K, where all molecules are detected. In addition, this emission is expected to trace the lowest temperature and thus the outermost radius at which the molecules start to appear. Previously, the disk was found to be rotating roughly with a Keplerian rotation due to a central mass of ∼0.25 $M_\odot$ (including the masses of the central protostar and the disk; Codella et al. 2014; Lee et al. 2017c).

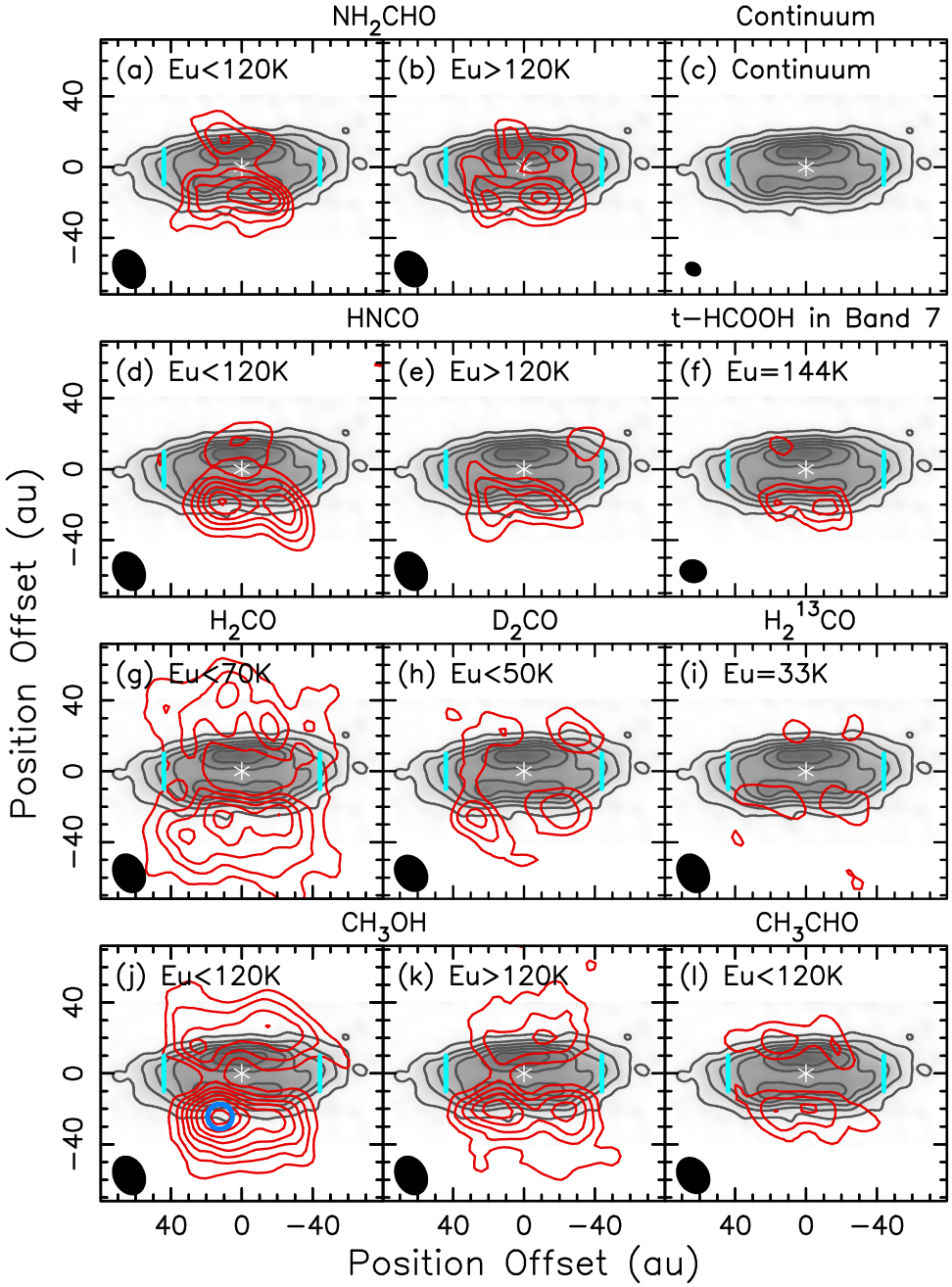


Figure 1. Total line intensity maps of NH_2CHO, HNCO, t-HCOOH, H_2CO, D_2CO, $H_2^{13}CO$, CH_3OH, and CH_3CHO (red contours) on top of the 1.33 mm continuum map (gray image with black contours) toward the HH 212 disk. The maps are rotated clockwise by ∼23° so that the disk is aligned horizontally for easy view. For the continuum, the contours start from 10 K with a step of 15 K. The line intensity maps are integrated over velocity within ∼4.0 km s^{-1} of the systemic velocity (which is ∼ 1.7 ± 0.1 km s^{-1} LSR Lee et al. 2014). As described in the text, we divided the lines into two ranges of upper-level energies: $E_u < 120$ K and $E_u > 120$ K, and then stacked them for each species for higher sensitivity. The asterisk marks the possible position of the central protostar. The vertical cyan lines mark the centrifugal barrier. The contours start at 3σ with a step of 2σ, where σ are (a) 1.5, (b) 0.8, (d) 2.1, (e) 1.3, (f) 4.0, (g) 2.4, (h) 2.6, (i) 3.4, (j) 1.6, (k) 1.8, and (l) 1.4 mJy $beam^{-1}$. The blue circle in (j) marks the emission peak used to derive the physical properties of CH_3OH.

Therefore, the associated Keplerian rotation curves (blue curves) are plotted here for comparison.

The emissions of these molecules trace the disk atmosphere within the CB and are thus enclosed by the Keplerian rotation curves. In the upper disk atmosphere, their emissions form roughly linear PV structures (as marked by the magenta lines), indicating that they arise from rings rotating at certain velocities. For edge-on rotating rings, the radial velocity observed along the line of sight is proportional to the position offset from the center, forming the linear PV structures. Interestingly, the PV structures of HNCO and t-HCOOH are aligned with those of NH_2CHO, and the PV structures of D_2CO are roughly aligned with those of CH_3OH. Except for these similarities, different molecules have different velocity gradients connecting to different locations of the Keplerian curves, indicating that they arise from rings at different disk radii. From the location of their PV structure on the Keplerian curve, we find that the disk radius of these molecules increases from ∼24 au for NH_2CHO/HNCO/t-HCOOH, to ∼36 au for CH_3CHO, to ∼40 au for CH_3OH/D_2CO, and then to ∼48 au

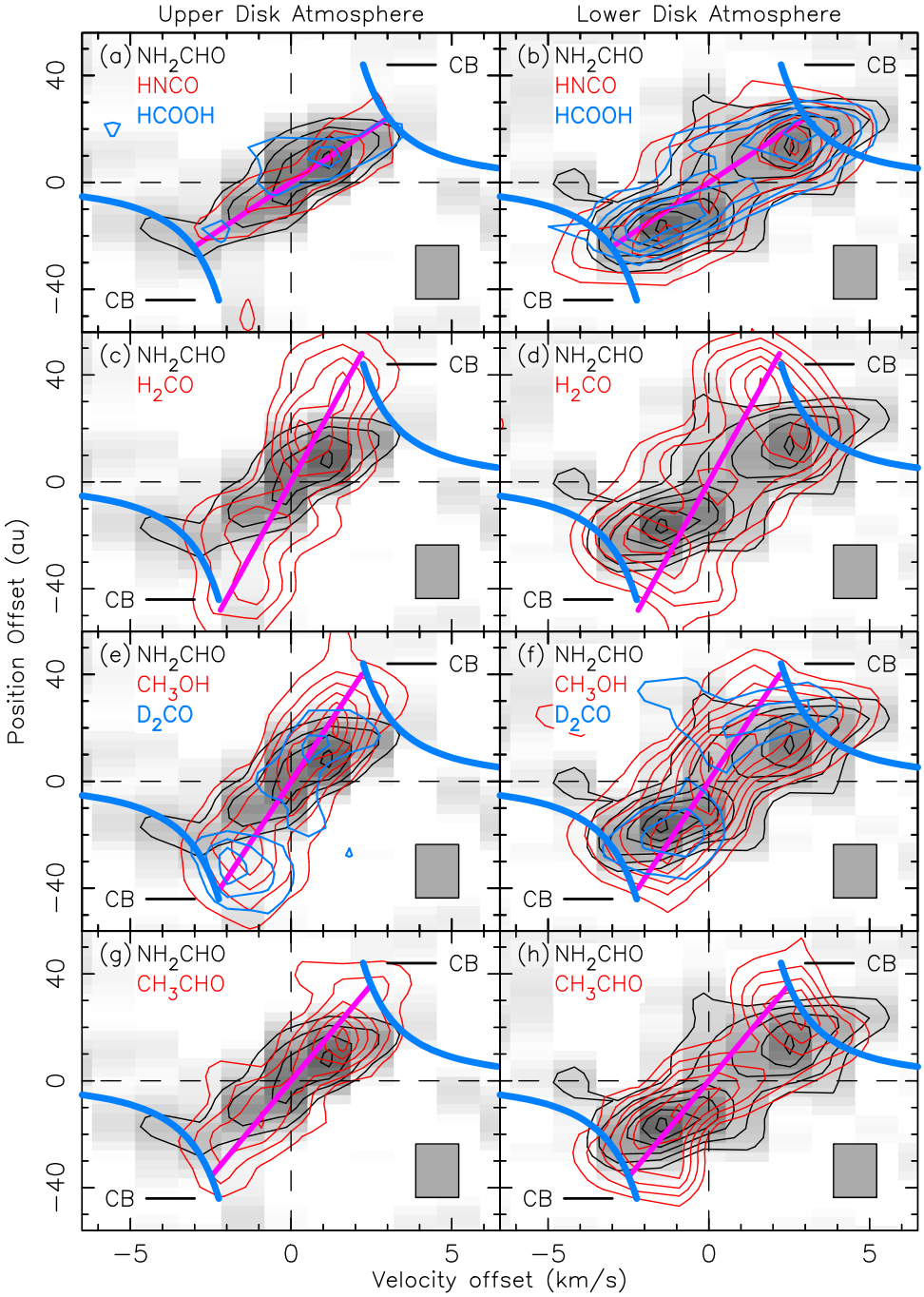


Figure 2. Position–velocity diagrams of various molecular lines cut across the upper and lower atmospheres of the disk. The contours start from 3σ with a step of 2σ, where σ are 0.36, 0.51, 0.70, 0.51, 0.43, 0.70, and 0.22 mJy beam^{-1} for NH_2CHO, HNCO, t-HCOOH, H_2CO, CH_3OH, D_2CO, and CH_3CHO, respectively. The vertical lines mark the systemic velocity. The horizontal lines mark the center of the atmosphere. We also plot the Keplerian rotation curves (blue curves) due to a central mass of 0.25 $M_\odot$ (Lee et al. 2017c). The magenta lines roughly mark the linear velocity gradients of the PV structures in the upper atmosphere.

for H_2CO. This trend is the same as the increasing order of the vertical height measured earlier for these molecules, indicating that the height increases with increasing radius, as expected for a flared disk in hydrostatic equilibrium. Plotting the velocity gradients in the upper disk atmosphere onto the lower disk atmosphere, we find that the emission detected in the upper disk atmosphere is actually only from the outer radius where their emission starts to appear, and the emission also extends radially inward to where NH_2CHO is detected. Since the near side of the disk is tilted slightly downward to the south, the emission in the upper disk atmosphere further in is lost due to the absorption against the bright and optically thick continuum emission of the disk surface (see Figure 9(b) in Lee et al. 2019). Note that for NH_2CHO/HNCO/t-HCOOH, there seems to be a small velocity shift of $\sim$0.5 km s^{-1} between the upper and lower disk atmosphere. This velocity shift could suggest an infall (or accretion) velocity of $\sim$0.25 km s^{-1}, which is $\sim$8% of the rotation velocity at $\sim$24 au. However, observations at higher spectral and spatial resolution are needed to verify this possibility.

3.3. Physical Properties in the Disk Atmosphere

In order to understand the nature and spatial origin of the detected methanol, we analyzed the observed methanol lines (Table 1) via a non-LTE Large Velocity Gradient (LVG) approach, using the code GRELVG, initially developed by Ceccarelli et al. (2003). We used the collisional coefficients of methanol with para-H_2, computed by Rabli & Flower (2010) between 10 and 200 K for the $J \leqslant 15$ levels and provided by the BASECOL database (Dubernet et al. 2012, 2013). We assumed an A-/E- CH_3OH ratio equal to 1. To compute the line escape probability as a function of the line optical depth we adopted the semi-infinite slab geometry (Scoville & Solomon 1974) and a linewidth equal to 4 km s^{-1}, following the observations.

We ran several grids of models to sample the χ^2 surface in the parameter space. Specifically, we varied the methanol column density N(A-CH_3OH) and N(E-CH_3OH) simultaneously from 2×10^{15} to 1×10^{19} cm^{-2} (with a step of a factor of 2), the H_2 density n_{H_2} from 10^6 to 10^9 cm^{-3} (with a step of a factor of 2) and the gas temperature T from 50 to 120 K (with a step of 5 K). We then fit the measured the velocity-integrated line intensities ($W = \int T_B dv$ with T_B being the brightness temperature) by comparing them with those predicted by the model, leaving N(A-CH_3OH) and N(E-CH_3OH), n_{H_2}, and T as free parameters. Given the limitation on the J level ($\leqslant$15), we used only seven of the twelve detected methanol lines with $E_u < 200$ K for the LVG fitting. We considered the line intensities at the emission peak (marked by a blue circle in Figure 1(j)) in the lower disk atmosphere, as listed in Table 1.

The results of the fit are shown in Figure 3. The best fit gives the following values, where the errors are estimated considering the 1σ confidence level and the uncertainties of $\sim$40% in our measurements: $N(CH_3OH) = N(A\text{-}CH_3OH) + N(E\text{-}CH_3OH) \sim 1.6^{+4.4}_{-0.8} \times 10^{18}$ cm^{-2}; $n_{H_2} \sim 10^9$ cm^{-3}, which should be the lower limit because it is in the LTE regime at this density; and $T \sim 75 \pm 20$ K. The lines are predicted to be all optically thick with the lowest line opacity $\tau \sim 1$ for the line at 234.699 GHz and the highest $\tau \sim 19$ for the line at 218.440 GHz, and $\tau = 3$–10 for the other lines. We also derived the excitation temperature and column density from the rotation diagram using the remaining five transition lines with $E_u > 200$ K (see Figure 3(c)), assuming optically thin emission and LTE (Goldsmith & Langer 1999). In particular, we fit the data with a linear equation, and then derived the temperature from the negative reciprocal of the slope and the column density from the y-intercept. We found that $T \sim 109 \pm 31$ K and $N(CH_3OH) = (1.4 \pm 0.7) \times 10^{18}$ cm^{-2}. Taking the mean values from the two methods, we have $T \sim 92^{+48}_{-37}$ K and $N(CH_3OH) = 1.5^{+4.5}_{-0.8} \times 10^{18}$ cm^{-2}. Notice that the previous LTE estimation of excitation temperature of CH_3OH and CH_2DOH together from the rotation diagram was pretty uncertain, with a value of 165 ± 85 K (Lee et al. 2017c), due to a large scatter of the data points. More importantly, the excitation temperature was also overestimated because almost all the lines had $E_u < 200$ K and were thus likely optically thick.

For less abundant molecules detected with a broad range of E_u, such as NH_2CHO and HNCO, the mean excitation temperature and column density of the molecular lines in the disk atmosphere can be roughly estimated from a rotation diagram assuming optically thin emission and LTE (Goldsmith & Langer 1999). We used the brighter emission in the lower disk atmosphere. Table 1 lists the integrated line intensities averaged over a rectangular region (with a size of 68 au $\times$ 20 au) that covers most of the emission in the lower atmosphere, measured with a cutoff of 2σ. Figure 4 shows the resulting rotation diagrams for NH_2CHO and HNCO. The blended lines of NH_2CHO are excluded from the diagram. The HNCO line at the lowest E_u (marked with an open square) seems to be optically thick with an intensity much lower than the line next down the E_u axis, and is thus excluded from the fitting. For NH_2CHO and HNCO, we fit the data points to obtain the temperature and column density. It is interesting to note that NH_2CHO and HNCO have roughly the same excitation temperature of $\sim 226 \pm 130$ K, although with a large uncertainty. On the other hand, since H_2CO, D_2CO, and CH_3CHO are only detected with a narrow range of $E_u < 120$ K and their emission can be optically thick there, we can not derive their excitation temperature from the rotation diagram. In addition, H_2CO and D_2CO are only detected with two lines. Also, $H_2^{13}CO$ is only detected with one line. Since D_2CO has roughly the same radial extent as CH_3OH, it is assumed to have an excitation temperature of 92 K, the same as that found for CH_3OH. Since H_2CO has a slightly larger radius than CH_3OH, it and its ^{13}C isotopologue $H_2^{13}CO$ are assumed to have an excitation of 60 K. CH_3CHO has a smaller radial extent than CH_3OH and is thus assumed to have an excitation temperature of 100 K.

The resulting excitation temperature and column density are listed in Table 2. In addition, the abundance of these molecules is also estimated by dividing the column density of the molecules by the mean H_2 column density derived from a dusty disk model (Lee et al. 2021b) in the same region, which is found to be $\sim 1.08 \times 10^{25}$ cm^{-2}. This disk model was constructed before to reproduce the continuum emission of the disk at $\lambda \sim 850$ μm (Lee et al. 2021b), and it can also roughly reproduce the continuum emission of the disk observed here at $\lambda \sim 1.33$ mm (Lin et al. 2021). Since H_2CO and D_2CO lines are each detected with two lines that are likely optically thick, their lines at higher E_u are used to derive the lower limit of their column density. Indeed, the H_2CO column density can be better derived from the $H_2^{13}CO$ line assuming $[^{12}C]/[^{13}C]$ ratio of $\sim$50, as estimated in the Orion Complex (Kahane et al. 2018). As can be seen from Table 2, the H_2CO column density derived this way is $\sim$3 times that derived from the H_2CO lines. Thus, the deuteration of H_2CO, i.e., the abundance ratio $[D_2CO]/[H_2CO]$, is $\gtrsim 0.053$. As for CH_3CHO, we fixed its temperature to 100 K by fixing the negative reciprocal of the slope in the linear equation and then derived its column density from the y-intercept of the linear fit to the rotation diagram, as shown in Figure 4(c).

4. Discussion

4.1. Lack of Molecular Emission in Disk Midplane

As discussed in Lee et al. (2017c, 2019), the lack of molecular emission in the disk midplane can be due to an exponential attenuation by the high optical depth of the dust continuum. Figure 5(a) shows the optical depth of the dust continuum at 1.33 mm derived from the dusty disk model that reproduced the thermal emission of the disk (Lee et al. 2021b). As can be seen, the optical depth is $\gtrsim 3$ toward the midplane within the CB, where no molecular emission is detected,

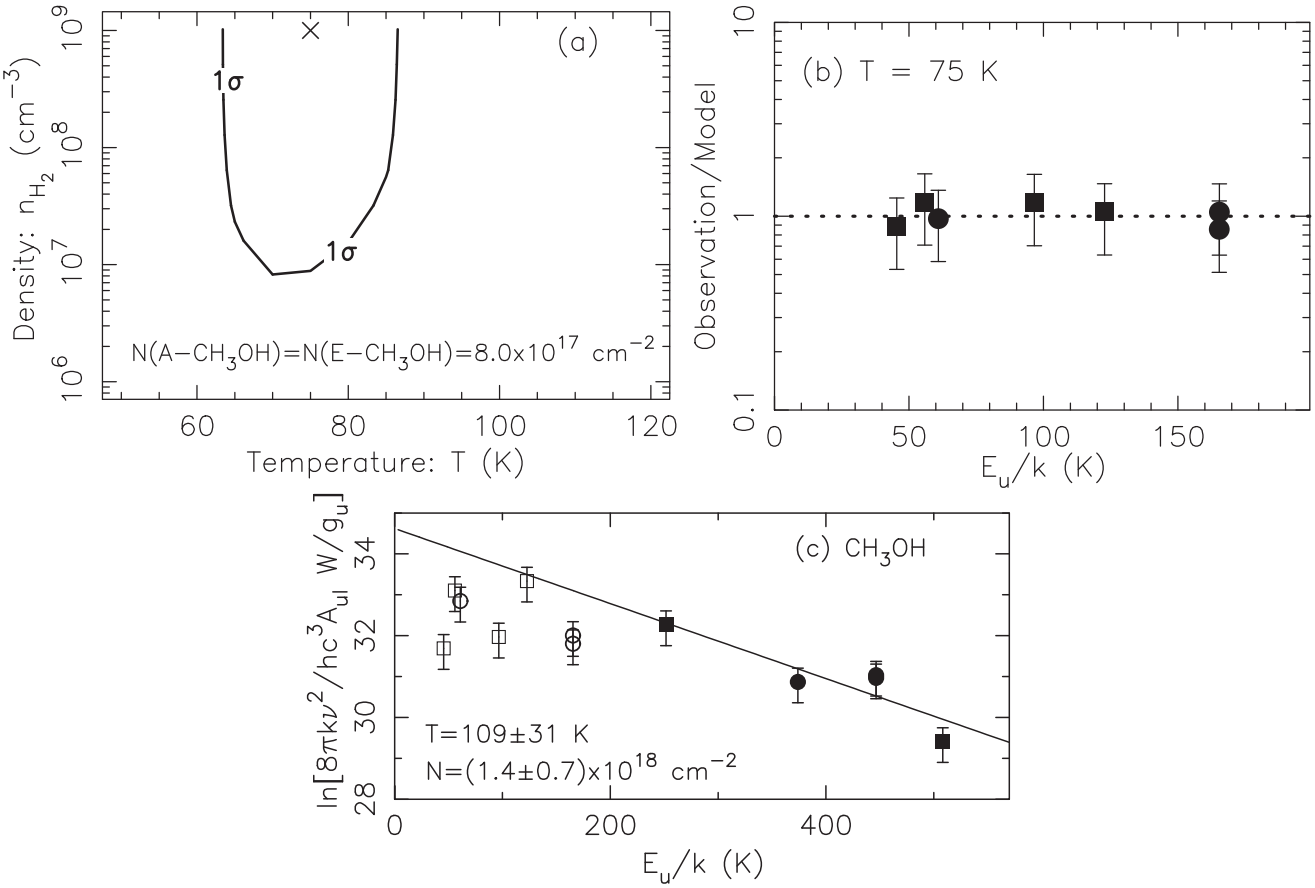


Figure 3. Physical properties of CH_3OH toward the disk atmosphere. (a) and (b) show the results of the non-LTE LVG analysis using the lines with $E_u < 200$ K with the GRELVG code (Ceccarelli et al. 2003), while (c) shows the result of the rotation diagram using the lines with $E_u > 200$ K. The line intensity is extracted from an emission peak in the lower disk atmosphere, as marked by a blue circle in Figure 1(j). (a) Density–Temperature χ^2 contour plot. The contour represents a 1σ confidence level, assuming the best-fit values of N(A-CH_3OH) and N(E-CH_3OH). The best-fit solution is marked by the cross. (b) The ratio between the observed line intensities (circles for A-type and squares for E-type) with those of the best fit as a function of E_u. (c) Rotation diagram of CH_3OH with the same symbols. The solid line is a linear fit to the data. The optically thick lines are marked with open squares and circles and excluded from the fitting.

supporting this possibility. The faint NH_2CHO and CH_3OH emission detected in the midplane likely comes from the upper and lower disk atmospheres due to the beam convolution. However, the H_2CO emission in the midplane near the CB (see Figure 1(g)) should be real detection because the optical depth of the dust continuum decreases to smaller than 3 at the edge.

4.2. Distribution of Molecules and Binding Energy

As discussed earlier, a stratification is seen in the distribution of molecules in the disk atmosphere, with the outer disk radius decreasing from H_2CO, to CH_3OH, to CH_3CHO, and then to NH_2CHO/HNCO/HCOOH, as shown in Figure 5(b) together with the temperature structure of the dusty disk model (Lee et al. 2021b). Similar stratification of H_2CO, CH_3CHO, and NH_2CHO has been seen toward the bow shock region B1 in the young protostellar system L1157 (Codella et al. 2017). That shock region is divided into three shock subregions, with shock 1 in the bow wing, shock 3 in the bow tip, and shock 2 in between. The authors interpreted that shock 1 is the youngest shock while shock 3 is the oldest. They found that the observed decrease in abundance ratio [CH_3CHO]/[NH_2CHO] from shock 3 to shock 2 and to shock 1 can be modeled if both NH_2CHO and CH_3CHO are formed in the gas phase.

Here in the HH 212 disk, since the temperature of the atmosphere is expected to increase inward toward the center of the disk (Figure 5(b)), the stratification in the distribution of these molecules could be related to their binding energy (BE; and thus sublimation temperature). Table 3 lists the recently computed BE for these molecules. For consistent comparison, we adopt the values obtained from similar methods on amorphous solid water ice (Ferrero et al. 2020; Ferrero & Grieco 2022). Since HNCO was not included in those studies, we adopt its value from Song & Kastner (2016). Notice that different methods can result in different BE, e.g., HCOOH was found to have a BE value of less than 5000 K on pure ice (Kruczkiewicz et al. 2021), significantly lower than that adopted here. As can be seen, the increasing order of the observed outer radius of NH_2CHO/t-HCOOH, CH_3OH, and H_2CO is consistent with the decreasing order of their BE, indicating that these molecules are thermally desorbed from the ice mantle on dust grains. Notice that this does not necessarily mean that these molecules are formed in the ice mantle, because the density in the disk is so high that even if the molecules are formed in the gas phase they freeze out quickly and are, therefore, only detected in regions where the dust temperature is larger than the sublimation temperature. As for HNCO and CH_3CHO, their outer radii do not fit into those of H_2CO, CH_3OH, and NH_2CHO based on their BE and they can form in the gas phase from other species. On the other hand, HNCO and HCOOH may come from the decomposition of the desorbed organic salts ($NH_4^+OCN^-$ and $NH_4^+HCOO^-$), which

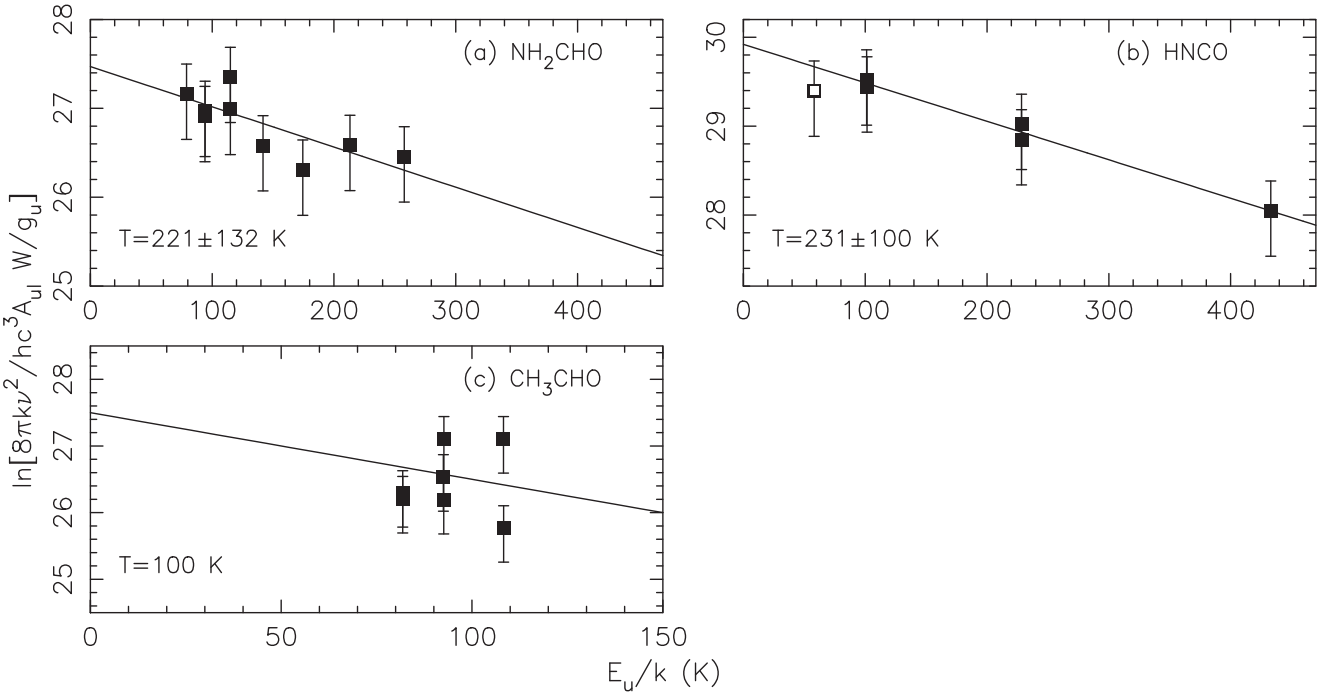


Figure 4. Rotation diagrams for molecular lines of NH_2CHO, HNCO, and CH_3CHO. The diagrams are derived from the line intensities in the lower disk atmosphere listed in Table 1. The error bars show the uncertainty in our measurements, which are assumed to be 40% of the data values. The solid line is a linear fit to the data. The blended lines of NH_2CHO are excluded from the diagram. The optically thick line of HNCO is marked with an open square and excluded from the fitting. For CH_3CHO, the temperature is fixed at 100 K.

Table 2
Column Densities and Abundances in the Lower Disk Atmosphere

Species	Excitation Temperature (K)	Column Density (cm^{-2})	Abundance[h]
CH_3OH[a]	92^{+48}_{-37}	$1.5^{+4.5}_{-0.8} \times 10^{18}$ cm^{-2}	$1.4^{+4.2}_{-0.7} \times 10^{-7}$
NH_2CHO[b]	221 ± 132	$(5.2 \pm 2.6) \times 10^{15}$	$(4.8 \pm 2.4) \times 10^{-10}$
HNCO[b]	231 ± 100	$(1.8 \pm 0.5) \times 10^{16}$	$(1.7 \pm 0.9) \times 10^{-9}$
H_2CO[c]	60±20[e]	$\gtrsim(1.4 \pm 0.7) \times 10^{16}$	$\gtrsim(1.3 \pm 0.7) \times 10^{-9}$
H_2CO[d]		$(4.5 \pm 2.3) \times 10^{16}$	$(4.2 \pm 2.1) \times 10^{-9}$
$H_2^{13}CO$	60 ± 20[e]	$(9.0 \pm 4.5) \times 10^{14}$	$(8.3 \pm 4.2) \times 10^{-11}$
D_2CO	92 ± 30[f]	$\gtrsim(2.4 \pm 1.2) \times 10^{15}$	$\gtrsim(2.2 \pm 1.1) \times 10^{-10}$
CH_3CHO	100 ± 50[g]	$(8.7 \pm 4.4) \times 10^{15}$	$(8.0 \pm 4.0) \times 10^{-10}$

Notes.
[a] Mean temperature and column density derived from non-LTE LVG calculation and rotation diagram.
[b] Temperature and column density derived from rotation diagram.
[c] Column density derived from H_2CO line.
[d] Column density derived from $H_2^{13}CO$ line, assuming $[^{12}C]/[^{13}C]$ ratio of 50.
[e] Temperature assumed to be 60 K.
[f] Mean temperature assumed to be the same as CH_3OH.
[g] Temperature assumed to be 100 K.
[h] Abundance derived by dividing the column densities of the molecules by the H_2 column density in the disk atmosphere, which is $\sim 1.08 \times 10^{25}$ cm^{-2} (see text).

have similar BE to that of NH_2CHO (Kruczkiewicz et al. 2021; Ligterink et al. 2018). Further work is needed to check this possibility.

Previously at $\sim 0\farcs15$ (60 au) resolution, Codella et al. (2018) detected deuterated water around the disk. Although the deuterated water was found to have an outer radius of $\sim$60 au, its kinematics was found to be consistent with that of the centrifugal barrier at $\sim$44 au. More importantly, since water has a BE similar to that of H_2CO (see Table 3), it is likely that water, like H_2CO, is also desorbed from the ice mantle on the dust grains. Thus the water snowline can be located around or slightly outside the centrifugal barrier.

4.3. Centrifugal Barrier and H_2CO and CH_3OH

The high deuteration of H_2CO (with $[D_2CO]/[H_2CO] \gtrsim 0.053$) and methanol (with $[CH_2DOH]/[CH_3OH] \sim 0.12$; Lee et al. 2019) supports that both are originally formed in ice. These ratios of $[D_2CO]/[H_2CO]$ and $[CH_2DOH]/[CH_3OH]$ are consistent with those found in prestellar cores to Class I sources (Mercimek et al. 2022), references therein. It is possible that H_2CO is formed by hydrogenation to CO frozen in the ice mantle on dust grains and then CH_3OH is formed from it with the addition of two H atoms (Charnley 2004). The derived kinetic temperature of CH_3OH agrees with the sublimation temperature, also supporting that the methanol is thermally desorbed into the gas phase. H_2CO and CH_3OH are detected with the outer radius near the CB where an accretion shock is expected as the envelope material flows onto the disk (Lee et al. 2017c), suggesting that they are desorbed into the gas phase due to the heat produced by the shock interaction. It is possible that they were already formed in the ice mantle on dust grains in the collapsing envelope stage and then brought into the disk (Herbst & van Dishoeck 2009; Caselli & Ceccarelli 2012). H_2CO has a lower sublimation temperature than CH_3OH, and thus can be desorbed into the gas phase further out beyond the CB. Interestingly, both H_2CO and CH_3OH also extend vertically away from the disk surface, and thus can also trace the disk wind as SO (Tabone et al. 2017; Lee et al. 2018, 2021a). In addition, since H_2CO has an outer radius

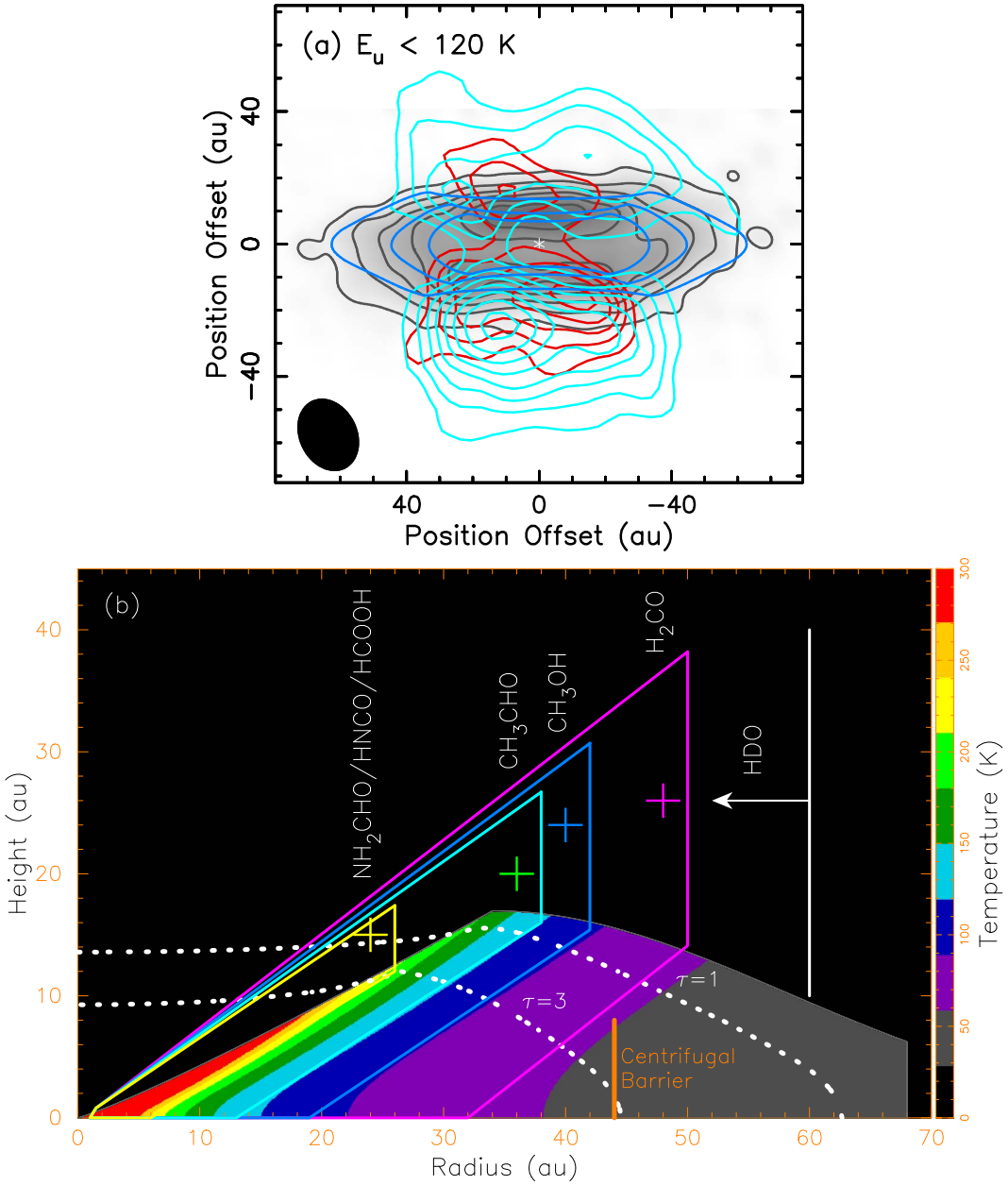


Figure 5. (a) Continuum map (black contours and gray image, same as Figure 1(c)), continuum optical depth (blue contours, with contour levels 1, 3, and 5) at $\lambda \sim 1.33$ mm (or 226 GHz), NH_2CHO (red contours, same as Figure 1(a)) and CH_3OH (cyan contours, same as Figure 1(j)) total line intensity maps. (b) Stratification of various molecules in the disk atmosphere plotted on the temperature structure of the dusty disk adopted from Lee et al. (2021b). The crosses mark the outer radius and vertical height measured from the observations. The upper limit of the outer radius of HDO estimated at 60 au resolution by Codella et al. (2018) is also marked.

outside the centrifugal barrier, it may also trace the wind from the innermost envelope transitioning to the disk, carrying away angular momentum from there.

4.4. Formamide, HNCO, and H_2CO

HNCO not only has similar spatial distribution and kinematics, but also has a similar excitation temperature to NH_2CHO, though with a large uncertainty. In addition, the abundance ratio of HNCO to NH_2CHO agrees well with the nearly linear abundance correlation found before across several orders of magnitude in molecular abundance (López-Sepulcre et al. 2019). All these suggest a chemical link between the two molecules. However, as discussed earlier, based on the BE sequence, HNCO itself is likely formed in the gas phase but not desorbed from the ice mantle, unless the BE of HNCO is significantly underestimated. In particular, although HNCO has a much lower BE than NH_2CHO, it is detected only in the inner and warmer disk where NH_2CHO is detected, but not detected in the outer part of the disk where the temperature is lower. Thus, our result implies that HNCO, instead of being the parent molecule, is likely a daughter molecule of NH_2CHO and formed in the gas phase. One possible reaction is $NH_2CHO+H \rightarrow HNCO$ (Haupa et al. 2019). It is also possible that HNCO is formed by destructive gas-phase ion–molecule interactions with amides (also larger amides than NH_2CHO; Garrod et al. 2008; Tideswell et al. 2010).

It has also been proposed that formamide can be formed from formaldehyde (H_2CO) in warm gas through the reaction $H_2CO+NH_2 \rightarrow NH_2CHO+H$ (Kahane et al. 2013; Vazart et al.

Table 3
Binding Energy (BE) and Sublimation Temperature (T_{sub}) in Amorphous Solid Water Ice

Species	Binding Energy (K)	T_{sub} (K)	Outer Radius (au)	References
CH_3CHO	2809-6038(4423)	48-102(75)	36	Ferrero+2022
H_2CO	3071-6194(4632)	52-104(78)	48	Ferrero+2020
HNCO	2400-8400(4800)	41-140(81)	24	Song & Kastner 2016
CH_3OH	3770-8618(6194)	64-144(104)	40	Ferrero+2020
HCOOH	5382-10559(7970)	91-176(133)	24	Ferrero+2020
NH_2CHO	5793-10960(8376)	97-183(140)	24	Ferrero+2020
NH_3	4314-7549(5931)	73-126(100)	⋯	Ferrero+2020
H_2O	3605-6111(4858)	61-103(82)	60[a]	Ferrero+2020

Note.
[a] The outer radius is given by that of HDO mapped at 60 au resolution (Codella et al. 2018). The numbers in the parenthesis are the mean values, except for HNCO, which is a value for maximum sublimation. The sublimation temperature (T_{sub}) is calculated for an age of 10^6 yr, appropriate for a young protoplanetary disk. Adopting a shorter time of 10^5 yr, appropriate for a Class 0/I protostellar system, would increase the sublimation temperature by a few degrees. Note that the computed BE values, notably those of acetaldehyde and ammonia, may be slightly at odds with the published experimental ones, which depend on the structure of the ices as well as the distribution of the species population on the ices. For this reason, we chose to stick to the BEs computed by the same authors, Ferrero et al., (with the exception of HNCO because these authors did not compute it), to make the comparison possibly more reliable.

2016; Codella et al. 2017; Skouteris et al. 2017). However, we find that H_2CO has a more extended distribution with different kinematics from formamide, and is thus unclear if it can be the parent molecule in the gas phase. Unfortunately, we have no information on the other reactant, NH_2. Very likely it is the product of sublimated NH_3 (Codella et al. 2017), whose binding energy (see Table 3) is larger than that of H_2CO, which may explain why formamide is not present where H_2CO is. In conclusion, based on the current observations, it is not possible to constrain the formation route of formamide in the disk atmosphere of HH 212. Nonetheless, our work has added precious information about the formation route of formamide in the disk atmosphere, complementing those in different environments, e.g., the L1157 shock (Codella et al. 2017).

We thank the anonymous reviewers for their insightful comments. This paper makes use of the following ALMA data: ADS/JAO.ALMA#2017.1.00712.S. ALMA is a partnership of ESO (representing its member states), NSF (USA), and NINS (Japan), together with NRC (Canada), NSC and ASIAA (Taiwan), and KASI (Republic of Korea), in cooperation with the Republic of Chile. The Joint ALMA Observatory is operated by ESO, AUI/NRAO, and NAOJ. C.-F.L. acknowledges grants from the Ministry of Science and Technology of Taiwan (MoST 107-2119-M-001-040-MY3, 110-2112-M-001-021-MY3) and the Academia Sinica (Investigator Award AS-IA-108-M01). C.Ce. and C.Co. acknowledge the funding within the European Union's Horizon 2020 research and innovation program, from the European Research Council (ERC), for the project "The Dawn of Organic Chemistry" (DOC), grant agreement No. 741002, and from the Marie Sklodowska-Curie for the project "Astro-Chemical Origins" (ACO), grant agreement No. 811312; the PRIN-INAF 2016 The Cradle of Life—GENESIS-SKA (General Conditions in Early Planetary Systems for the rise of life with SKA); the PRIN-MUR 2020 BEYOND-2P (Astrochemistry beyond the second-period elements), Prot. 2020AFB3FX.

ORCID iDs

Chin-Fei Lee https://orcid.org/0000-0002-3024-5864
Claudio Codella https://orcid.org/0000-0003-1514-3074
Cecilia Ceccarelli https://orcid.org/0000-0001-9664-6292
Ana López-Sepulcre https://orcid.org/0000-0002-6729-3640

References

Bianchi, E., Codella, C., Ceccarelli, C., et al. 2019, MNRAS, 483, 1850
Biver, N., Bockelee-Morvan, D., Moreno, R., et al. 2015, SciA, 1, 1500863
Caselli, P., & Ceccarelli, C. 2012, A&ARv, 20, 56
Cazaux, S., Tielens, A. G. G. M., Ceccarelli, C., et al. 2003, ApJL, 593, L51
Ceccarelli, C., Maret, S., Tielens, A. G. G. M., et al. 2003, A&A, 410, 587
Ceccarelli, C., Caselli, P., Herbst, E., et al. 2007, in Protostars and Planets V, ed. V. B. Reipurth, D. Jewitt, & K. Keil (Tucson, AZ: Univ. Arizona Press), 47
Ceccarelli, C., Caselli, P., Fontani, F., et al. 2017, ApJ, 850, 176
Charnley, S. B. 2004, AdSpR, 33, 23
Charnley, S. B., & Rodgers, S. D. 2008, SSRv, 138, 59
Codella, C., Cabrit, S., Gueth, F., et al. 2014, A&A, 568, L5
Codella, C., Ceccarelli, C., Cabrit, S., et al. 2016, A&A, 586, L3
Codella, C., Ceccarelli, C., Caselli, P., et al. 2017, A&A, 605, L3
Codella, C., Bianchi, E., Tabone, B., et al. 2018, A&A, 617, A10
Coutens, A., Jørgensen, J. K., van der Wiel, M. H. D., et al. 2016, A&A, 590, L6
Dubernet, M.-L., Alexander, M. H., Ba, Y. A., et al. 2013, A&A, 553, A50
Dubernet, M.-L., Nenadovic, L., & Doronin, N. 2012, in ASP Conf. Ser. 461, ADASS XXI, ed. P. Ballester, D. Egret, & N. P. F. Lorente (San Francisco, CA: ASP), 335
Enrique-Romero, J., Rimola, A., Ceccarelli, C., et al. 2022, ApJS, 259, 39
Ferrero, S., Zamirri, L., Ceccarelli, C., et al. 2020, ApJ, 904, 11
Ferrero, S., Grieco, F., Ibrahim Mohamed, A.-S., et al. 2022, MNRAS, in press
Garrod, R. T., Widicus Weaver, S. L., & Herbst, E. 2008, ApJ, 682, 283
Goldsmith, P. F., & Langer, W. D. 1999, ApJ, 517, 209
Haupa, K. A., Tarczay, G., & Lee, Y.-P. 2019, JAChS, 141, 11614
Herbst, E., & van Dishoeck, E. F. 2009, ARA&A, 47, 427
Hsu, S.-Y., Liu, S.-Y., Liu, T., et al. 2022, ApJ, 927, 218
Imai, M., Sakai, N., Oya, Y., et al. 2016, ApJL, 830, L37
Kahane, C., Ceccarelli, C., Faure, A., et al. 2013, ApJL, 763, L38
Kahane, C., Jaber Al-Edhari, A., Ceccarelli, C., et al. 2018, ApJ, 852, 130
Kruczkiewicz, F., Vitorino, J., Congiu, E., et al. 2021, A&A, 652, A29
Lee, C.-F., Hirano, N., Zhang, Q., et al. 2014, ApJ, 786, 114
Lee, C.-F., Li, Z.-Y., Ho, P. T. P., et al. 2017c, ApJ, 843, 27
Lee, C.-F., Li, Z.-Y., Ho, P. T. P., et al. 2017b, SciA, 3, e1602935
Lee, C.-F., Li, Z.-Y., Codella, C., et al. 2018, ApJ, 856, 14
Lee, C.-F., Codella, C., Li, Z.-Y., et al. 2019, ApJ, 876, 63
Lee, C.-F., Tabone, B., Cabrit, S., et al. 2021a, ApJL, 907, L41
Lee, C.-F., Li, Z.-Y., Yang, H., et al. 2021b, ApJ, 910, 75
Ligterink, N. F. W., Terwisscha van Scheltinga, J., Taquet, V., et al. 2018, MNRAS, 480, 3628
Lin, Z.-Y.-D., Lee, C.-F., Li, Z.-Y., Tobin, J. J., & Turner, N. J. 2021, MNRAS, 501, 1316
López-Sepulcre, A., Balucani, N., Ceccarelli, C., et al. 2019, ESC, 3, 2122
López-Sepulcre, A., Sakai, N., Neri, R., et al. 2017, A&A, 606, A121

Manigand, S., Jørgensen, J. K., Calcutt, H., et al. 2020, A&A, 635, A48
Mercimek, S., Codella, C., Podio, L., et al. 2022, A&A, 659, A67
Noble, J. A., Theule, P., Congiu, E., et al. 2015, A&A, 576, A91
Rabli, D., & Flower, D. R. 2010, MNRAS, 406, 95
Rimola, A., Skouteris, D., Balucani, N., et al. 2018, ESC, 2, 720
Saladino, R., Crestini, C., Pino, S., Costanzo, G., & Di Mauro, E. 2012, PhLRv, 9, 84
Scoville, N. Z., & Solomon, P. M. 1974, ApJL, 187, L67
Skouteris, D., Vazart, F., Ceccarelli, C., et al. 2017, MNRAS, 468, L1
Song, L., & Kastner, J. 2016, PCCP, 18, 29278
Tabone, B., Cabrit, S., Bianchi, E., et al. 2017, A&A, 607, L6
Tideswell, D. M., Fuller, G. A., Millar, T. J., et al. 2010, A&A, 510, A85
Vazart, F., Calderini, D., Puzzarini, C., Skouteris, D., & Barone, V. 2016, J. Chem. Theory Comput., 12, 5385